

Observation of Coherent Quantum Tunneling of a Massive Atomic Cluster with 435 u

Han Zhang,^{1,2,*} Yong-Kui Wang,^{1,*} Yi Zheng,^{1,*} Hai-Tao Bai,¹ and Bing Yang^{1,2,†}

¹*Department of Physics and Guangdong Basic Research Center of Excellence for Quantum Science, Southern University of Science and Technology, Shenzhen 518055, China*

²*Quantum Science Center of Guangdong-Hong Kong-Macao Greater Bay Area, Shenzhen 518045, China*

(Dated: February 11, 2025)

Tunneling is a genuine quantum phenomenon typically observed in low-mass particles such as electrons. However, it fades rapidly as mass increases due to the exponential decay of the matter-wave penetration depth. Cooling atoms to nanokelvin temperatures enhances their matter wave characteristics. Here, we report the observation of coherent quantum tunneling of a bonded cluster composed of 5 ultracold rubidium-87 atoms, collectively forming a massive object of 435 u. Using a double-well superlattice, integer occupancy states are prepared, with atoms bonded via strong on-site interactions. We demonstrate that the exponential base of tunneling strength can be tuned to approach unity, drastically reducing its decay for heavier masses and enabling a scalable strategy. Moreover, tunneling is harnessed to create spatially separated Schrödinger-cat states (~ 320 nm apart), achieving quantum enhancement in measurements. This work markedly raises the mass threshold for quantum tunneling and paves the way for quantum metrology with massive particles.

Introduction. Quantum tunneling is a fundamental quantum effect arising from the matter-wave properties of objects [1]. The tunneling of electrons is extensively utilized in devices such as scanning tunneling microscopes, and superconducting qubits for quantum computing. For a general object with mass m and kinetic energy K traversing a square barrier of height V_0 and thickness d , the transmission probability is proportional to $\exp(-\gamma\sqrt{m})$ [2], where $\gamma = 2\sqrt{2(V_0 - K)}d/\hbar$ (\hbar is the reduced Planck constant). This relation indicates that the tunneling strength decays exponentially with increasing mass m , leading to a fundamental question: to what extent can quantum tunneling be realized on macroscopic objects with large masses.

The matter-wave de Broglie wavelength can be enhanced by cooling objects to low temperatures, as demonstrated in ultracold atoms, where matter waves exhibit large-scale interference [3]. In this context, ultracold atoms can tunnel through barriers with widths on the order of hundreds of nanometers, with such barriers often created using laser light. Tunneling effects have been observed in systems involving single atoms and atom pairs [4–11]. In atomic superfluids, where particles interact weakly, collective tunneling emerges as a Josephson-like effect [12–16]. However, the dependence of tunneling strength on mass has rarely been explored, and exponential decay is generally considered an intrinsic constraint. Although low temperatures enhance matter wave properties, the exponential form of decay continues to pose substantial challenges for observing tunneling in large-mass objects, such as those with masses exceeding that of uranium, the heaviest stable atom at 238 u.

Here, we propose that multiple bonded bosonic atoms can form a cluster that collectively tunnels through a barrier as a single entity. For bonded ultracold atoms, we identify a regime in which tunneling strength follows a decay remarkably slower than the typical exponential

behavior. Specifically, when the mutual binding energy U (between two atoms) exceeds the single-atom kinetic energy J_0 but is smaller than the barrier height (i.e., $V_0 \gg |U| > J_0$), a cluster of n atoms can tunnel through the barrier via a high-order perturbation process with a strength scaling as J_0^n/U^{n-1} . When $J_0/U \sim 1$, collective tunneling of atomic clusters remains substantial, with minimal amplitude suppression. In this regime, the tunneling strength of large-mass clusters deviates from the conventional exponential decay, approaching that of individual atoms as the exponential base nears unity.

In this work, we generate atomic Mott insulators with a controllable integer filling factor in optical lattices. Strong repulsive on-site interactions bond the atoms into clusters, enabling them to enter the collective tunneling regime. We improve the stability of the superlattice potential and markedly extend the coherence time of spatially separated entangled states. Through time-resolved measurements, we directly observe the coherent tunneling dynamics of atomic clusters with up to 5 atoms, corresponding to 435 atomic mass units. The tunneling strength exhibits a slight decrease with increasing mass, providing a unique approach to scaling up the mass of the tunneling object. Additionally, for large mass clusters, tunneling induces entanglement of position states, serving as a valuable resource for measuring spatially distributed fields. We demonstrate improved sensitivity in measuring sub-micrometer energy shifts, outperforming the precision limit of classical methods.

Theoretical descriptions. We consider a double-well system as the minimal platform for studying the tunneling effect, as illustrated in Fig. 1a. For strongly bonded atoms with attractive interaction $|U| \gg V_0$, $U < 0$, the atoms form a molecular cluster with mass $m = n \cdot m_0$, leading to a smaller matter-wave packet and an exponential reduction in tunneling strength, scaling as $\exp(-\gamma\sqrt{m})$. In the weakly bound regime ($|U| \ll V_0$),

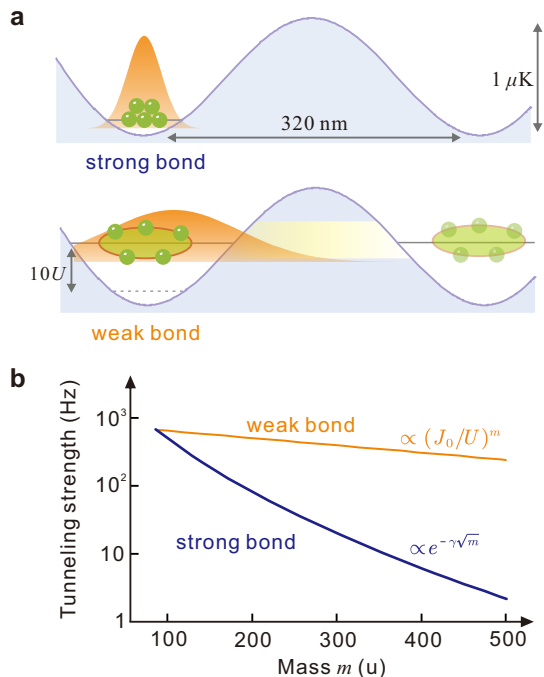


FIG. 1: Quantum tunneling of bonded atoms. (a) Tunneling of two types of clusters. In a double-well potential with a barrier height of $1 \mu\text{K}$ and a width of 320 nm , strongly bonded clusters feature smaller matter-wave packets. In contrast, for weakly bonded clusters, the matter wave resembles that of individual particles and can penetrate into the adjacent well. The repulsive on-site interactions elevate the energy levels, introducing an energy penalty to suppress other tunneling processes. (b) Tunneling strengths and cluster mass. The tunneling strength is calculated based on the ^{87}Rb atom. Assuming the system is in the strongly bonded regime, the strength is expected to decrease exponentially, as indicated by the blue line. For weakly bonded atoms, it exhibits a near-unity scaling with increasing mass (orange line).

the interaction can be treated as a pseudopotential, allowing the atomic wavefunction to approximate that of a single atom [17–19]. This provides an alternative high-order perturbative path for the tunneling of clusters from the state $|n, 0\rangle$ to $|0, n\rangle$ through virtual states $|n - i, i\rangle$, where $i = 1, 2, \dots, n - 1$. Repulsive interaction ($U > 0$) raises the zero-energy level, suppressing the single-atom tunneling by creating an energy mismatch between the initial state and intermediate virtual states. The effective tunneling of this high-order process is given by $J_n = \alpha_n J_0^n / U^{n-1}$, where α_n accounts for the energy-shifts of virtual states relative to $|n, 0\rangle$ in multiple of U .

We create double-well potentials and realize weakly bonded clusters using an optical superlattice. Ultracold bosons in the optical lattices can be described by the ground-band Bose-Hubbard model [20],

$$\hat{H}_0 = \sum_j \left[-J_0 (\hat{a}_j^\dagger \hat{a}_{j+1} + \text{h.c.}) + \frac{U}{2} \hat{n}_j (\hat{n}_j - 1) + \varepsilon_j \hat{n}_j \right], \quad (1)$$

where \hat{a}_j^\dagger (\hat{a}_j) denotes creation (annihilation) operator at site j , with $\hat{n}_j = \hat{a}_j^\dagger \hat{a}_j$ as the atom number operator. The term ε_j represents the on-site energy and chemical potential. In this system, two-body repulsive on-site interactions lead to the binding energy term [17]. Under this model, a superfluid-to-Mott-insulator phase transition can yield a uniform region with an integer atom number per site [4, 20], providing an ideal starting point for studying quantum tunneling.

By adjusting the double-well superlattice potentials [5, 21, 22], we reach the regime $V_0 \gg U > J_0$. As illustrated in Fig. 1a, we set the barrier height to $V_0/k_B = 1 \mu\text{K}$, the binding energy to $U/k_B = 40 \text{ nK}$, and the single atom tunneling to $J_0/k_B = 32 \text{ nK}$, achieving the weakly bonded condition. The tunneling strength as a function of mass is shown in Fig. 1b, reaching an experimentally accessible regime. To characterize the tunneling dynamics of bonded atoms, we can use a simplified two-mode model,

$$\hat{H}_c = -J_n \left[(\hat{a}_L^\dagger)^n (\hat{a}_R)^n + \text{h.c.} \right], \quad (2)$$

where the notation L/R denote the corresponding operators acting on the atoms at the left or right sites, respectively.

Experiment. The experiment starts with a nearly pure Bose-Einstein condensate of ^{87}Rb atoms, containing $\sim 2 \times 10^5$ atoms in the $|F = 1, m_F = -1\rangle$ state. The atoms are loaded into a single layer of pancake-shaped standing waves along the z -axis, with the atom number in this quasi-two-dimensional (2D) system adjustable via further evaporation (see Methods). This 2D gas is then adiabatically loaded into a square optical lattice in the $x - y$ plane. Along the y -axis, the lattice is created using counter-propagating lasers with a wavelength of $\lambda_s = 767 \text{ nm}$, while along the x -axis, a superlattice composed of lasers with wavelengths of λ_s (short-lattice) and $2\lambda_s$ (long-lattice) divides the trapped atoms into a series of double wells. The intensity maxima of these two lattice patterns are aligned, creating a balanced double-well superlattice configuration, as shown in Fig. 2a. The barrier height V_0 can be finely tuned by adjusting the lattice depths, and the barrier width is slightly less than $\lambda_s/2$.

We initialize the system by utilizing the integer filling property of the Mott insulator and a site-resolved atom manipulation technique. In this superlattice, we implement a cooling method for the Mott insulators by transferring entropy to nearby superfluid reservoirs [22]. The central filling factor n can be tuned from 1 to 5, with the corresponding temperatures measured between $3.7(2) \text{ nK}$ and $5.6(5) \text{ nK}$ (see Methods). The repulsive on-site interaction is around $U/h = 835(6) \text{ Hz}$, binding the particles together during the collective tunneling. Despite the strong interactions, three-body loss is relatively low, with the $1/e$ lifetime of the sample at $n = 5$ reaching

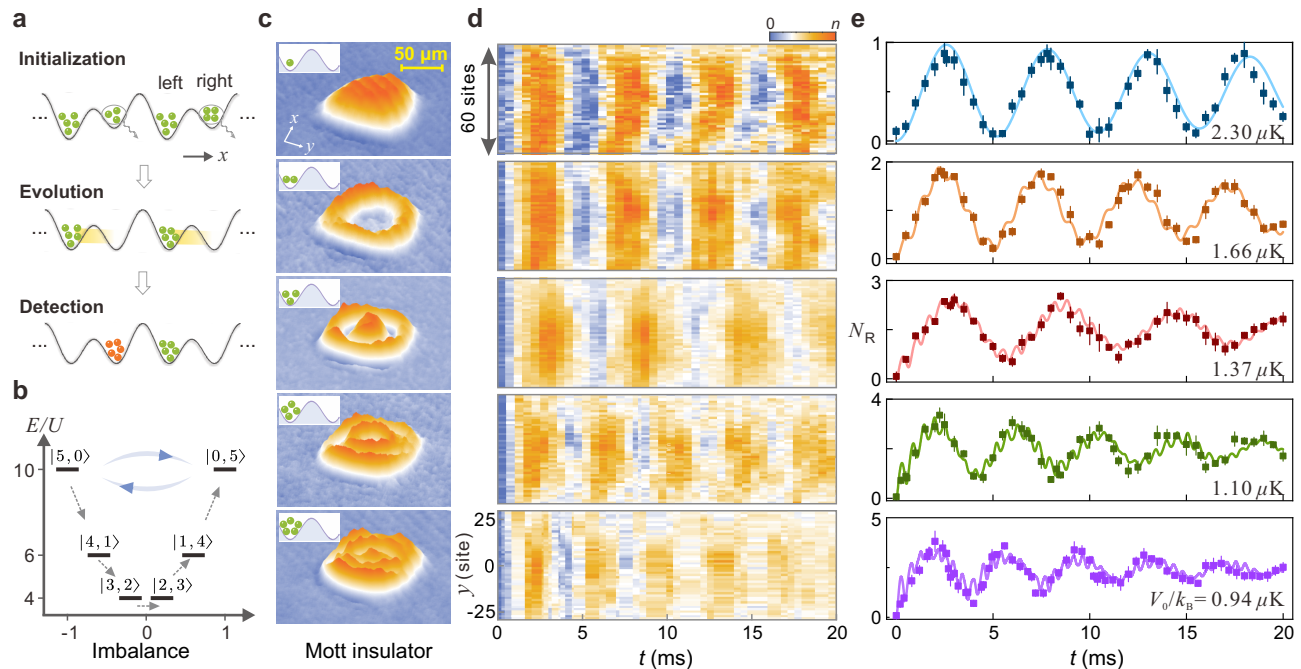


FIG. 2: Quantum tunneling dynamics. (a) Experimental sequence. The atoms are initialized using a cooling technique, followed by the removal of the right-site atoms, which serve as thermal reservoirs. During the evolution stage, the atomic clusters tunnel through the barrier in a balanced double-well potential. The quantum state is measured by selectively detecting the atoms on the right site, yielding the value N_R . (b) Energy spectrum at $J_0 \ll U$ and high-order tunneling process. For bonded atoms in the $|5, 0\rangle$ state, tunneling to the $|0, 5\rangle$ state occurs via a fifth-order process, linked by 4 intermediate virtual states between them. (c) Mott insulators with central fillings of 1 to 5. The density distributions are obtained through parity-projection measurements. In a harmonic trap, the shell structures of the Mott insulator states are clearly revealed. The insets indicate the population in the central region of the lattice. (d) Time-resolved observations of tunneling dynamics. *In situ* measurements are used to detect the time evolution and spatial distribution of the atomic clouds. The signal is averaged over 14 sites along the x -axis. (e) Coherent tunneling of atomic clusters. Data points represent the spatial average of N_R over the central 14 sites in (d). The barrier heights are labeled in the lower right corner of each plot. Experimental data points are shown alongside theoretical predictions (solid lines), with each measurement averaged over 5 repetitions; error bars indicate standard deviations.

3.2(2) s. To prepare the initial state with atoms occupying only the left sites, we selectively flip the internal states of the right-site atoms and subsequently remove them using resonant light.

We monitor the tunneling dynamics of bonded clusters in an array of isolated double wells. In the insulating state, tunneling is suppressed by setting high barriers in all directions. Along the x -direction, the long-lattice depth is kept at $8.87(4)E_r$ to prevent inter-well tunneling between adjacent double wells. Here, $E_r = \hbar^2/(2m_0\lambda_s^2)$ denotes the recoil energy, and m_0 is the atomic mass of ^{87}Rb . For double-well systems in the $|n, 0\rangle$ state, we lower the barrier and enable atoms to tunnel through. After a set interval, we rapidly raise the barrier to halt the tunneling dynamics and prepare for detection. Figure 2b shows the energy spectrum of a 5-atom bonded cluster in the Fock state basis, where tunneling is effectively a fifth-order perturbation process. In the balanced double well, the states $|5, 0\rangle$ and $|0, 5\rangle$ are degenerate, while each intermediate state has a lower energy, acting as virtual states that do not noticeably populate during the evo-

lution. Since maintaining the balanced configuration is critical to keeping the $|5, 0\rangle$ and $|0, 5\rangle$ states resonant, we stabilize the energy bias $\Delta \equiv \varepsilon_R - \varepsilon_L$ between wells to $2.5(1) \times 10^{-4}$ level relative to V_0 .

We measure quantum states by selectively detecting the atom number on the left or right sites using *in situ* absorption imaging. The density distributions of the initial states, projected onto the odd-even parity, are shown in Fig. 2c, revealing characteristic shell structures of the atomic Mott insulators. After the tunneling dynamics, we flip the right-site atoms to the $|F = 2, m_F = -2\rangle$ state and then detect the quantum mechanical expectation values N_R . Fig. 2d presents the time-resolved measurements, where the tunneling dynamics exhibit pronounced coherent oscillations over 20 ms. A spatially inhomogeneous distribution across 60 lattice sites emerges, with faster oscillations at the edges. This variation is attributed to the Gaussian intensity profile of the lattice beams and the spatial inhomogeneity of the atomic density distribution.

To quantify the tunneling dynamics, we focus on

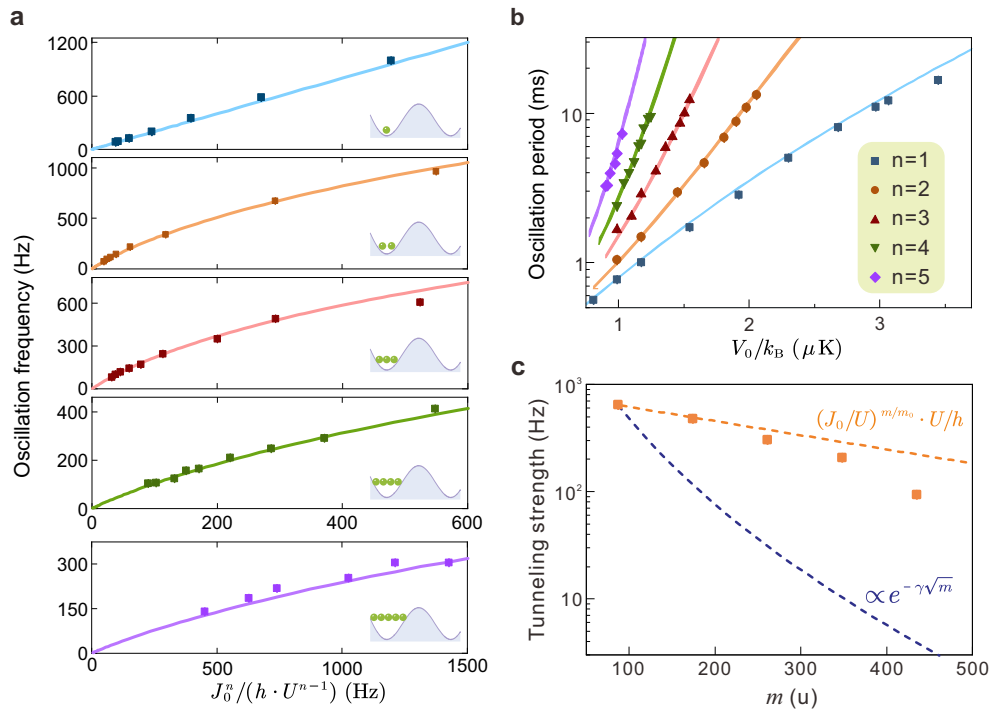


FIG. 3: Scaling of tunneling strength. (a) Oscillation frequencies of tunneling dynamics. The frequencies of tunneling atomic clusters are extracted from the data, exemplified in Fig. 2e. These frequencies are presented as a function of the Hubbard parameters in the form of J_0^n/U^{n-1} . Solid lines represent theoretical calculations based on accurately calibrated Hubbard parameters. (b) Oscillation periods and barrier height. A logarithmic plot is used to illustrate the exponential dependence of the period on the barrier height. Further analysis reveals a linear dependence of the exponent on cluster size n . Shaded areas, though barely visible, represent theoretical results accounting for lattice potential uncertainties. (c) Tunneling strength and mass. Dashed reference lines indicate near-unity scaling $(J_0/U)^{m/m_0}$ (orange) and exponential scaling $e^{-\gamma\sqrt{m}}$ (blue). Measurements at a fixed lattice potential show tunneling strengths for clusters of varying n , closely following near-unity scaling, with deviations attributed to prefactors in the perturbation model. Error bars in this figure denote standard deviations.

the central region of the system, where the interaction strengths and filling factors are uniform. From the measurements in Fig. 2e, we extract the dominant oscillation frequency, amplitude, and coherence time. In the single-atom case, the tunneling oscillation is a full-amplitude sinusoidal pattern, indicating high-fidelity initialization and precise control. For atomic clusters, the oscillation amplitudes reflect that the dynamics are driven by multi-particle effects. To explore the decoherence mechanism, we adjust V_0 to make the oscillation frequencies of different states comparable. The oscillations undergo decay as n increases, following nearly a $1/n$ dependence, suggesting that decoherence arises from the cumulative effects on individual atoms (see Methods). We theoretically calculate the dynamics using exact diagonalization methods, incorporating extended Hubbard terms [23]. In the $J_0/U \sim 1$ regime, we observe small-amplitude, higher-frequency oscillations superimposed on the main oscillations, resulting from incomplete suppression of other tunneling orders in perturbation theory. The calculation includes the phenomenological decay rate and accounts for finite-temperature induced occupation imperfections.

From the oscillation frequencies and the Hubbard pa-

rameters J_0 and U , we determine the scaling of the tunneling strength. According to perturbation theory, when $J_0/U \ll 1$, the tunneling strength is proportional to $\alpha_n J_0^n/U^{n-1}$. In the regime $J_0/U \sim 1$, the exponential base J_0/U approaches unity, while coupling to intermediate states in high-order processes slightly reduces the coefficient α_n . We theoretically calculate the frequencies and plot the results in Fig. 3a. In a wide range of coupling strengths, the oscillation frequency exhibits an almost linear dependence on J_0^n/U^{n-1} , with an n -dependent prefactor. Experimental data agree with theoretical predictions, clearly illustrating the scaling of tunneling strength for atomic clusters.

While the mass-dependent scaling is tunable, the bare tunneling rate J_0 still follows an exponential decay with increasing V_0 (since $\gamma \propto \sqrt{V_0}$ by neglecting the kinetic energy of cold atoms). This exponential behavior is evident for clusters of varying mass, as shown in Fig. 3b. When atoms form clusters, the decay is further amplified by a factor of n , as reflected in the steeper slope of the tunneling period. For heavier clusters, the experimental regime becomes more constrained as V_0 rises, further corroborating the bonded tunneling behavior of atoms.

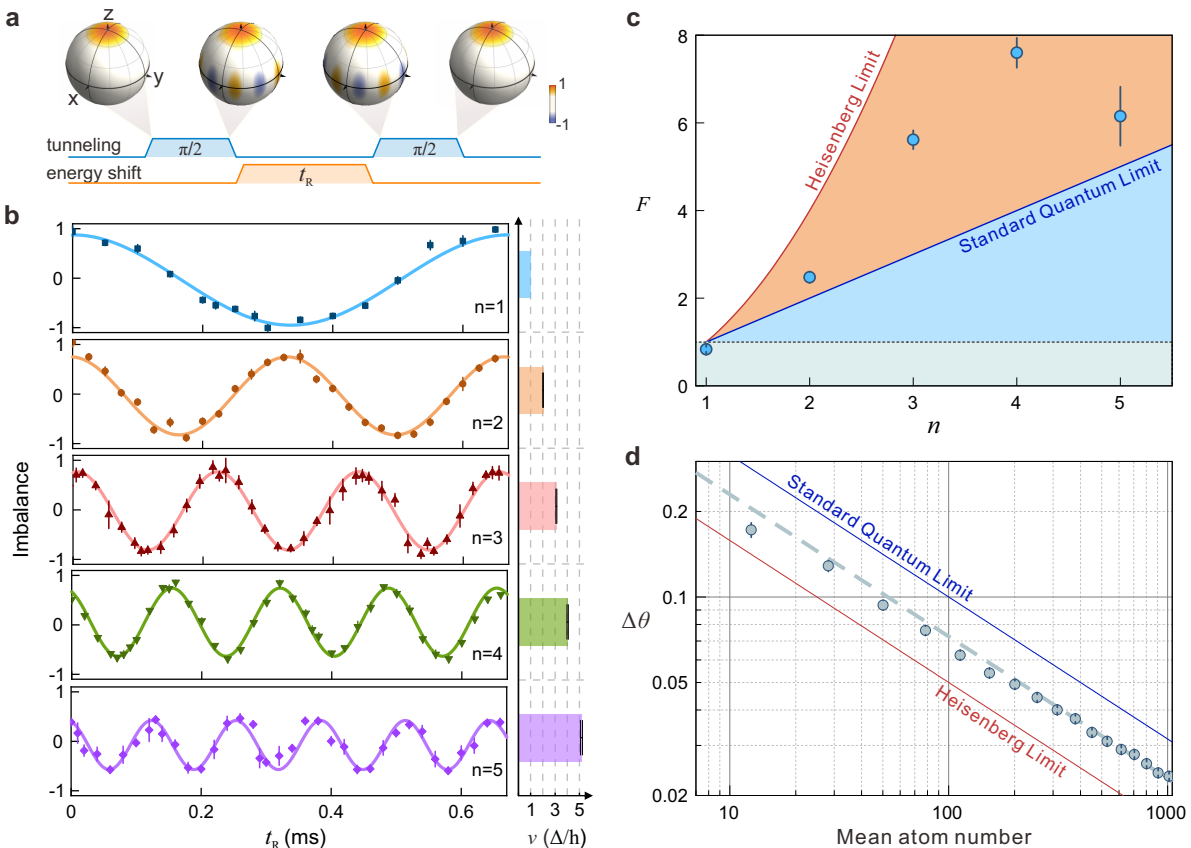


FIG. 4: Interferometry with Schrödinger cat states. (a) Ramsey interferometer. We represent the quantum states on the Bloch sphere with the Wigner distribution. Tunneling of bonded atoms generates an entangled state, exemplified by the NOON state for $n = 5$. This state evolves under a site-dependent energy shift, which rotates its phase by $\theta = \pi/5$ (as an example). In the detection stage, a second tunneling event acts as an equivalent $\pi/2$ -pulse in this Ramsey interferometer. (b) Detecting an energy shift with NOON states. The atom number imbalance between the left and right sites, expressed as $(N_R - N_L) / (N_R + N_L)$, is used to track the evolution of the state under the Ramsey sequence. Solid lines represent sinusoidal fits, and the oscillation frequencies are given in units of Δ/h , as shown in the right panel. The mean values of imbalance are slightly shifted from 0 due to other filling components in the Mott insulator. Each data point is averaged over at least 5 repetitions, and error bars denote standard errors. (c) Fisher information. We extract the oscillation amplitude from the measurements shown in (b) and calculate the Fisher information for each state. The Heisenberg limit scales as $F = n^2$ (red line), the standard quantum limit is $F = n$ (blue line), and the dashed line denotes the detection limit for a single-atom superposition state. (d) Precision measurements with the $n = 4$ NOON state. We count atoms in different spatial regions containing varying numbers of double-well units. The results show power-law dependence (dashed blue line) and increased sensitivity as the atom number grows.

We set the barrier height of the double well to $V_0/k_B = 0.99(1) \mu\text{K}$ and examine the scaling of tunneling strength with the mass of ultracold clusters. Our experiment focuses on the weakly bonded regime, with the Hubbard parameters set to $U/h = 835(6) \text{ Hz}$ and $J_0/h = 641(10) \text{ Hz}$. As shown in Fig. 3c, the measured tunneling strength follows a slow decay, aligning with the theoretical model. Since the factor α_n is not included in the theoretical guiding curve, the deviation is primarily attributed to its reduction for larger n , as derived from perturbation theory described by Eq. 2. Considering the boson enhancement effect, the tunneling strength acquires prefactors of $2/3$ and $5/24$ for clusters with $n = 4$ and $n = 5$, respectively. This modification does not alter the overall scaling of the tunneling strength, which can be

further facilitated by setting $J_0/U \gtrsim 1$. Since the energy penalty for lower-order tunneling processes lies between $(n-1)U$ and $n(n-1)U/2$, increasing J_0 close to the minimum energy gap, $(n-1)U$, has small impact on the n -atom tunneling amplitude, allowing the atoms to tunnel collectively (see Methods). The achieved coherence time and oscillation amplitude indicate considerable potential for further scaling up the system with more atoms.

Precision measurements. Quantum superposition states emerge during coherent tunneling dynamics, with the state at a quarter oscillation period expressed as $(|n, 0\rangle + i|0, n\rangle) / \sqrt{2}$. This state represents a maximally entangled Schrödinger cat state, commonly referred to as a NOON state [24, 25]. Due to the spatial separation of the massive atoms in $|n, 0\rangle$ and $|0, n\rangle$, these states

are highly sensitive to spatial variations in energy shifts, making them ideal for precision measurements. The inherent correlations in the entangled states enhance the sensitivity (denoted as $\Delta\theta$) for detecting the superposition phase [26, 27]. For an ideal NOON state, this sensitivity reaches the Heisenberg limit, $\Delta\theta = 1/n$, surpassing the standard quantum limit, $\Delta\theta = 1/\sqrt{n}$. Compared to NOON states in photonic systems [28, 29] or spatially non-separated qubits, spatially distributed massive entanglement offers the unique potential to probe mass-sensitive fields and atom-sensitive interactions.

We implement a Ramsey interferometer to probe a sub-micron effective magnetic gradient generated by the optical superlattice [30]. As shown in Fig. 4a, tunneling is harnessed to generate entanglement and detect the accumulated phase, analogous to the $\pi/2$ -pulse in the Ramsey interferometer protocol. The energy shift Δ between the left and right sites induces a single-atom phase accumulation over time t_R , described by $\theta = t_R\Delta/\hbar$. This evolution drives the entangled state into the form $[|n, 0\rangle + e^{i(n\theta+\pi/2)}|0, n\rangle]/\sqrt{2}$. The entangled state is visualized on the Bloch sphere, where a rotation of $2\pi/n$ restores the state, highlighting the enhanced phase sensitivity of n -atom entanglement.

Fig. 4b shows the detection results obtained using quantum superposition states. The single-particle oscillation frequency is measured to be $\Delta/h = 1.49(2)$ kHz, corresponding to the energy shift between adjacent wells. For clusters containing n atoms, the oscillation frequency scales linearly with n , providing additional evidence for the formation of n -atom NOON states via tunneling. We utilize Fisher information F to assess the measurement precision, as shown in Fig. 4c, where the four-atom cluster exhibits the most significant enhancement. Here, the Fisher information and phase sensitivity exceed the standard quantum limit by 2.8(2) dB and 1.4(1) dB, respectively. Furthermore, multiple copies of the entangled state are employed to improve the measurement precision, achieving a phase sensitivity of 0.023(1), which reflects the relative energy, with 254 copies of the four-body NOON state (see Fig. 4d).

Some experiments have realized Schrödinger cat states, ranging from massive superposition states [31–34] to nearly massless entangled states, including spin-entangled states [35–38]. In regimes where the de Broglie wavelength remarkably exceeds the atomic scale, particularly on the order of the laser wavelength, our experiment achieves a matter-wave cat state with a matter-wave wavelength of 320 nm. To our knowledge, the 435 u entangled cluster represents the largest realization of a massive quantum superposition with spatially discernible separation.

Conclusion and Outlook. Our experiment demonstrates that bonded atoms with a total mass of 435 u can undergo quantum tunneling as a single entity. Unlike the well-established exponential decay of tunneling strength

with increasing mass, we have developed a method to scale up the mass of the cluster and observed a near-unity scaling behavior, indicating the feasibility of extending to larger clusters. By improving system coherence and leveraging multichannel amplification [6, 10], we can potentially scale up to incorporate even more atoms. This achievement contributes to our understanding of quantum tunneling in large-mass objects and open a pathway to addressing the fundamental question of how large a mass can exhibit tunneling effects. The resulting quantum superposition states offer valuable applications for quantum metrology [27], particularly in measuring mass-sensitive fields such as gravitational field. The scaled-up massive entangled clusters with large spatial separations could be employed to test fundamental wave-function collapse models [39]. Furthermore, the high-order interactions in this strongly correlated system could give rise to novel quantum phases [23], offering new possibilities for quantum simulations [40, 41].

Acknowledgments. We thank J. Halimeh, P. Hauke, S. Jochim, J.-W. Pan, B. Wu, P. Zoller, and our colleagues at SUSTech for insightful discussions. This work is supported by the National Key R&D Program of China (Grant No. 2022YFA1405800), NNSFC (Grant No. 12274199), Shenzhen Science and Technology Program (Grant No. KQTD20240729102026004), Guangdong Major Project of Basic and Applied Basic Research (Grant No. 2023B0303000011) and Guangdong Provincial Quantum Science Strategic Initiative (Grant No. GDZX2304006, Grant No. GDZX2405006,).

* These authors contributed equally to this work.

† e-mail: yangbing@sustech.edu.cn

- [1] Razavy, M. *Quantum theory of tunneling* (World Scientific, 2013).
- [2] MacColl, L. A. Note on the transmission and reflection of wave packets by potential barriers. *Phys. Rev.* **40**, 621–626 (1932).
- [3] Andrews, M. R. *et al.* Observation of interference between two Bose condensates. *Science* **275**, 637–641 (1997).
- [4] Greiner, M., Mandel, O., Esslinger, T., Hansch, T. W. & Bloch, I. Quantum phase transition from a superfluid to a Mott insulator in a gas of ultracold atoms. *Nature* **415**, 39–44 (2002).
- [5] Fölling, S. *et al.* Direct observation of second-order atom tunnelling. *Nature* **448**, 1029–1032 (2007).
- [6] Meinert, F. *et al.* Observation of many-body dynamics in long-range tunneling after a quantum quench. *Science* **344**, 1259–1262 (2014).
- [7] Kaufman, A. M. *et al.* Two-particle quantum interference in tunnel-coupled optical tweezers. *Science* **345**, 306–309 (2014).
- [8] Preiss, P. M. *et al.* Strongly correlated quantum walks in optical lattices. *Science* **347**, 1229–1233 (2015).
- [9] Murmann, S. *et al.* Two fermions in a double well: Ex-

- ploring a fundamental building block of the Hubbard model. *Phys. Rev. Lett.* **114**, 080402 (2015).
- [10] Yang, B. *et al.* Observation of gauge invariance in a 71-site Bose–Hubbard quantum simulator. *Nature* **587**, 392–396 (2020).
- [11] Impertro, A. *et al.* Local readout and control of current and kinetic energy operators in optical lattices. *Phys. Rev. Lett.* **133**, 063401 (2024).
- [12] Cataliotti, F. S. *et al.* Josephson junction arrays with Bose-Einstein condensates. *Science* **293**, 843–846 (2001).
- [13] Albiez, M. *et al.* Direct observation of tunneling and nonlinear self-trapping in a single Bosonic Josephson junction. *Phys. Rev. Lett.* **95**, 010402 (2005).
- [14] Kwon, W. J. *et al.* Strongly correlated superfluid order parameters from dc Josephson supercurrents. *Science* **369**, 84–88 (2020).
- [15] Luick, N. *et al.* An ideal Josephson junction in an ultracold two-dimensional Fermi gas. *Science* **369**, 89–91 (2020).
- [16] Ramos, R., Spierings, D., Racicot, I. & Steinberg, A. M. Measurement of the time spent by a tunnelling atom within the barrier region. *Nature* **583**, 529–532 (2020).
- [17] Winkler, K. *et al.* Repulsively bound atom pairs in an optical lattice. *Nature* **441**, 853–856 (2006).
- [18] Bloch, I., Dalibard, J. & Zwirger, W. Many-body physics with ultracold gases. *Rev. Mod. Phys.* **80**, 885–964 (2008).
- [19] Lewenstein, M., Sanpera, A. *et al.* *Ultracold Atoms in Optical Lattices: Simulating quantum many-body systems* (OUP Oxford, 2012).
- [20] Jaksch, D., Bruder, C., Cirac, J. I., Gardiner, C. W. & Zoller, P. Cold bosonic atoms in optical lattices. *Phys. Rev. Lett.* **81**, 3108 (1998).
- [21] Sebby-Strabley, J., Anderlini, M., Jessen, P. S. & Porto, J. V. Lattice of double wells for manipulating pairs of cold atoms. *Phys. Rev. A* **73**, 033605 (2006).
- [22] Yang, B. *et al.* Cooling and entangling ultracold atoms in optical lattices. *Science* **369**, 550–553 (2020).
- [23] Dutta, O. *et al.* Non-standard Hubbard models in optical lattices: a review. *Rep. Prog. Phys.* **78**, 066001 (2015).
- [24] Sanders, B. C. Quantum dynamics of the nonlinear rotator and the effects of continual spin measurement. *Phys. Rev. A* **40**, 2417–2427 (1989).
- [25] Lee, H., Kok, P. & Dowling, J. P. A quantum Rosetta stone for interferometry. *J. Mod. Opt.* **49**, 2325–2338 (2002).
- [26] Braunstein, S. L. & Caves, C. M. Statistical distance and the geometry of quantum states. *Phys. Rev. Lett.* **72**, 3439–3443 (1994).
- [27] Pezzé, L., Smerzi, A., Oberthaler, M. K., Schmied, R. & Treutlein, P. Quantum metrology with nonclassical states of atomic ensembles. *Rev. Mod. Phys.* **90**, 035005 (2018).
- [28] Walther, P. *et al.* De Broglie wavelength of a non-local four-photon state. *Nature* **429**, 158–161 (2004).
- [29] Afek, I., Ambar, O. & Silberberg, Y. High-NOON states by mixing quantum and classical light. *Science* **328**, 879–881 (2010).
- [30] Yang, B. *et al.* Spin-dependent optical superlattice. *Phys. Rev. A* **96**, 011602 (2017).
- [31] Arndt, M. *et al.* Wave–particle duality of C₆₀ molecules. *Nature* **401**, 680–682 (1999).
- [32] Kovachy, T. *et al.* Quantum superposition at the half-metre scale. *Nature* **528**, 530–533 (2015).
- [33] Fein, Y. Y. *et al.* Quantum superposition of molecules beyond 25 kDa. *Nat. Phys.* **15**, 1242–1245 (2019).
- [34] Bild, M. *et al.* Schrödinger cat states of a 16-microgram mechanical oscillator. *Science* **380**, 274–278 (2023).
- [35] Monroe, C., Meekhof, D. M., King, B. E. & Wineland, D. J. A “Schrödinger cat” superposition state of an atom. *Science* **272**, 1131–1136 (1996).
- [36] Wang, C. *et al.* A Schrödinger cat living in two boxes. *Science* **352**, 1087–1091 (2016).
- [37] Omran, A. *et al.* Generation and manipulation of Schrödinger cat states in Rydberg atom arrays. *Science* **365**, 570–574 (2019).
- [38] Song, C. *et al.* Generation of multicomponent atomic Schrödinger cat states of up to 20 qubits. *Science* **365**, 574–577 (2019).
- [39] Bassi, A., Lochan, K., Satin, S., Singh, T. P. & Ulbricht, H. Models of wave-function collapse, underlying theories, and experimental tests. *Rev. Mod. Phys.* **85**, 471–527 (2013).
- [40] Daley, A. J. *et al.* Practical quantum advantage in quantum simulation. *Nature* **607**, 667–676 (2022).
- [41] Halimeh, J. C., Aidelburger, M., Grusdt, F., Hauke, P. & Yang, B. Cold-atom quantum simulators of gauge theories. *Nat. Phys.* (2025).
- [42] Dai, H.-N. *et al.* Four-body ring-exchange interactions and anyonic statistics within a minimal toric-code Hamiltonian. *Nat. Phys.* **13**, 1195–1200 (2017).
- [43] Mitchell, M. W., Lundeen, J. S. & Steinberg, A. M. Super-resolving phase measurements with a multiphoton entangled state. *Nature* **429**, 161–164 (2004).
- [44] Nagata, T., Okamoto, R., O’Brien, J. L., Sasaki, K. & Takeuchi, S. Beating the standard quantum limit with four-entangled photons. *Science* **316**, 726–729 (2007).
- [45] Zhang, J. *et al.* NOON states of nine quantized vibrations in two radial modes of a trapped ion. *Phys. Rev. Lett.* **121**, 160502 (2018).

METHODS AND SUPPLEMENTARY MATERIALS

GENERATION OF ULTRACOLD ATOMIC CLUSTER

We generate ultracold atomic clusters by cooling ^{87}Rb atoms to the quantum degenerate regime, followed by binding the atoms in optical lattices. Using laser cooling and evaporative cooling techniques, we achieve a nearly pure Bose-Einstein condensate with $\sim 2 \times 10^5$ atoms in the $5S_{1/2} |F=1, m_F=-1\rangle$ state. The condensate is then compressed along the z -direction with an elliptical laser beam, resulting in a Thomas-Fermi radius of $\sim 2 \mu\text{m}$. The atoms are adiabatically loaded into a single layer of a pancake-shaped optical superlattice, which is formed by the overlap of two interference patterns from 1064 nm and 532 nm lasers, intersecting at an angle of 9.3° . As shown in Fig. S1, the standing wave period along the z -axis for the 532 nm interference is $3.3 \mu\text{m}$, while the 1064 nm lattice has a period twice as large. The superlattice is carefully designed and controlled to ensure the atoms are loaded into a single two-dimensional (2D) system. The superlattice trap frequency along the z -axis is $2\pi \times 5.65(4)$ kHz, ensuring that the system enters the 2D regime. Due to some heating during compression, we perform additional evaporative cooling to reduce the temperature in this 2D system.

To enter the strongly interacting regime, we load the atoms into optical lattices along the x - and y -axes (see Fig. S1). The optical lattice along the x -axis is a superlattice, with a potential given by $V(x) = V_s \cos^2(2\pi x/\lambda_s) - V_l \cos^2(2\pi x/\lambda_l + \varphi)$, where $\lambda_s = 767$ nm and $\lambda_l = 1534$ nm are the wavelengths of the short- and long-lattices, and V_s and V_l are their respective depths. The phase φ determines the superlattice structure. To ensure precise phase control, the short-lattice laser is generated by up-converting the long-lattice laser, where the relative frequencies of the two lasers are stabilized to within a Hertz-level precision. The phase φ is finely tuned by adjusting the relative frequency between the two lasers using acousto-optical modulators. Additionally, the 767 nm laser has a linewidth below 10 kHz. Compared to previous work in Ref. [22], the frequency fluctuations between the superlattice lasers have been essentially eliminated, with a suppression of several orders of magnitude.

We utilize the integer filling property of the Mott insulator states to deterministically prepare n -atom bonded clusters. The Mott insulator phase is realized by driving a quantum phase transition governed by the Hubbard model in the 2D system. To improve the filling factor of the Mott insulator, we apply additional cooling in the optical lattices, as demonstrated in Ref. [22]. Following

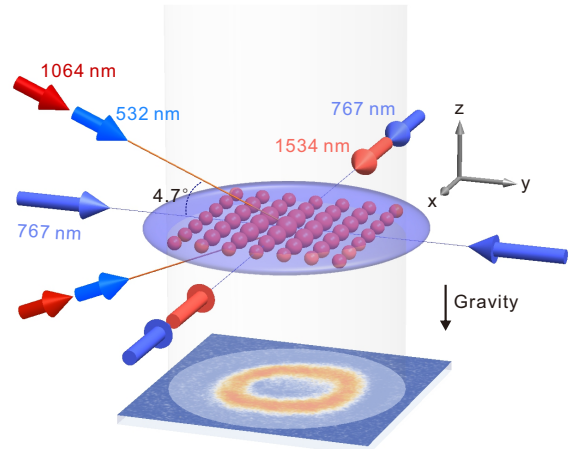


FIG. S1: Sketch of the experimental setup. A single layer of a 2D system is created by loading ultracold atoms into a pancake-shaped lattice formed by the interference of 532 nm and 1064 nm laser beams. Retro-reflected laser beams in the x and y directions create the corresponding optical lattices. A blue-detuned lattice with a wavelength of 767 nm is applied in both the x and y directions, while a red-detuned lattice with a wavelength of 1534 nm is used to create a double-well superlattice along the x -direction. This setup enables the superfluid-to-Mott insulator transition in the 2D atomic gas. Atomic clouds are imaged via absorption imaging along the z -axis, which is aligned with the gravity direction.

the cooling sequence, a parity-projection measurement is employed to assess the temperature and filling factor of the Mott insulator states. This technique involves a photoassociation process to excite atomic pairs into unstable molecular states. We use a laser red-detuned 13.6 cm^{-1} from the D2 line, frequency-locked via a transfer cavity, to drive the transition of atoms to the $v = 17$ vibrational state in the 0_g^- channel. After applying the laser light for 20 ms, the filling factor n is projected into its modulus of 2, yielding the odd or even parity.

We detect the *in situ* atomic density using highly saturated absorption imaging. In the Hubbard regime, where sites are occupied by multiple atoms, resolving the 2D cloud requires fast, high-saturation imaging. We precisely calibrate the saturation effect and apply a modified Beer-Lambert law to determine the atomic density. Additionally, Mott insulator states with integer filling factors serve as a further validation for imaging calibration. As shown in Fig. S2(a), the shell structure of the Mott insulator is observed for different filling factors. Under

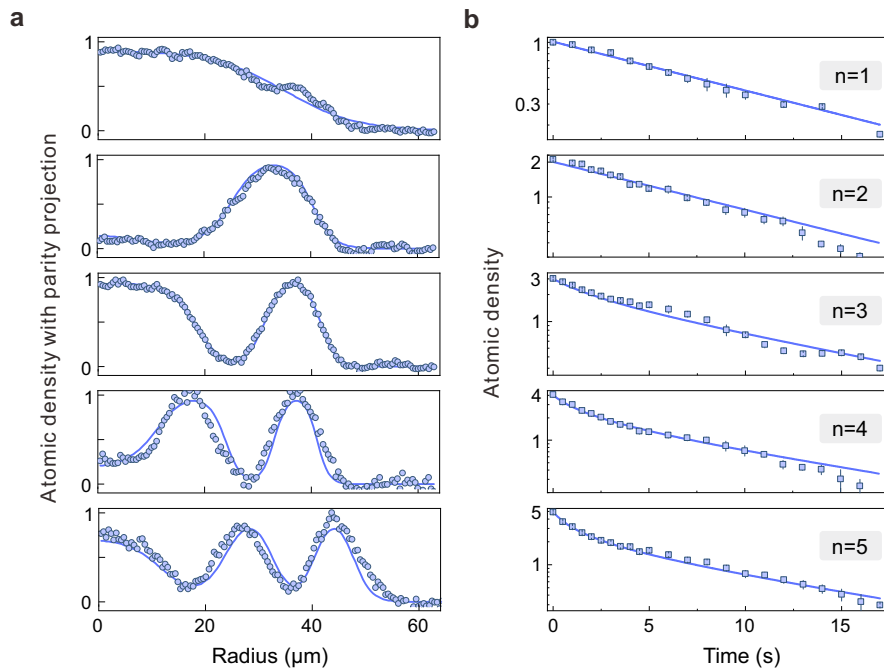


FIG. S2: Atomic Mott insulator and lifetimes of bonded clusters. (a) Atomic density profiles of the Mott insulator in the harmonic trap are shown for central filling factors $n = 1, 2, \dots, 5$. The atomic filling is mapped onto its odd or even parity using the photoassociation excitation method. From the atomic densities in Fig. 2c, we select a line-cut region specifically for analysis, avoiding deformation caused by imperfections in the trapping envelope. The shell structure of the Mott insulator is clearly visible in the density profiles. Fitting results (solid line) based on the local density approximation for the atomic limit ($U/J_0 \rightarrow \infty$) are shown, which allow for the determination of the atomic temperature. (b) Lifetime measurements of n -atom clusters. Starting from near-uniform filling of different Mott insulator states, we monitor the atom number decay in deep optical lattices. For single and double occupancy, the decay follows an exponential form. For $n \geq 3$, three-body losses contribute to a rapid initial decay. The solid lines represent fits accounting for both one-body and three-body losses.

the local density approximation, the temperature of the atomic ensemble is inferred from the *in situ* density distribution. Due to the inhomogeneity of the atomic density, we focus on the central, uniform region of the cloud for measuring the tunneling dynamics, where the atoms consistently form n -atom bonded atomic clusters.

The atomic clusters have sufficiently long lifetimes to allow for the observation of tunneling dynamics. We measure the lifetime of the Mott insulator states at various filling factors by holding the atoms in deep optical lattices and monitoring the decay of atom number, as shown in Fig. S2(b). We identify one-body and three-body losses as the primary decay mechanisms, with measured rates of $9.5(3) \times 10^{-2} \text{ s}^{-1}$ for one-body loss and $1.6(3) \times 10^{-31} \text{ cm}^6 \text{ s}^{-1}$ for three-body loss (considering only the ground-band extension of the atomic Wannier function). The one-body loss is attributed to background collisions in the vacuum and light scattering from the optical lattices. The $1/e$ lifetime of the $n = 1$ Mott state is $10.5(3) \text{ s}$, with the short-lattice detuned by only 13 nm from the D2 line contributing to the single-particle loss. Notably, the three-body loss is relatively weak for ^{87}Rb atoms. The $1/e$ lifetimes for the samples at $n = 3, 4, 5$ are $6.3(5) \text{ s}$, $4.3(2) \text{ s}$, and $3.2(2) \text{ s}$, respectively. These lifetimes are

three orders of magnitude longer than the tunneling period shown in Fig. 2e. Since the cold atomic ensemble contains a sufficient number of atoms, the combination of strong tunneling and relatively low decay rates creates a favorable regime for studying the tunneling dynamics of bonded atoms and opens possibilities for extending cluster sizes to even larger masses.

ATOM MANIPULATIONS AND TUNNELING EFFECT

We conduct quantum tunneling experiment in a balanced double-well superlattice with a phase setting of $\varphi = 0$, as shown in Fig. 2. To selectively manipulate atoms in the left or right wells, we introduce a spin-dependent optical superlattice [30]. By tuning the polarization of the short-lattice laser, we apply a vector light shift to the atoms, followed by a microwave pulse to selectively flip the spin state on the right lattice sites, from $|F = 1, m_F = -1\rangle$ to $|F = 2, m_F = -2\rangle$. The magnetic bias field is stabilized at 0.82 Gauss with a precision of $\sim 0.1 \text{ mG}$. A rapid adiabatic passage pulse is employed to flip the spin state, ensuring high-fidelity state prepa-

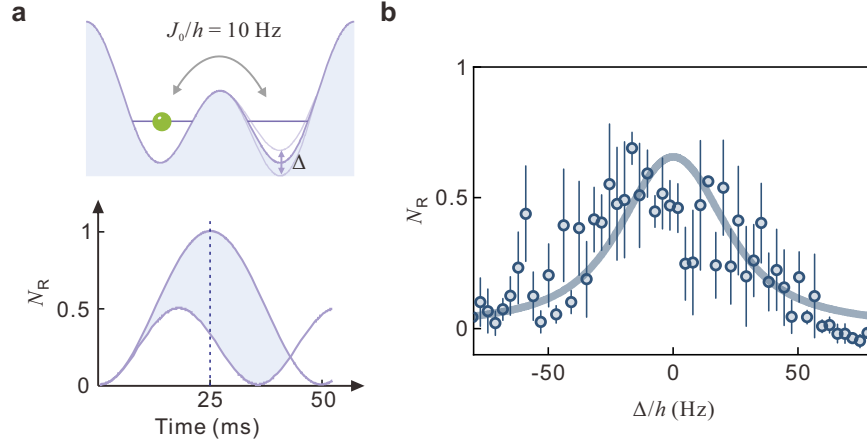


FIG. S3: Detecting energy fluctuations between left and right wells. (a) Measurement procedure. The energy shift Δ is probed using single-atom tunneling. With a tunneling strength of $J_0/h = 10.0(2)$ Hz, any small fluctuation in Δ induces detuning in the Rabi coupling, affecting the tunneling between the two wells. The amplitude of the atom population is measured at half a tunneling period. (b) Spectroscopy of energy fluctuations. Spectroscopic measurements reveal fluctuations in the atom number on right sites, attributed to noise in Δ . The spectroscopy of atom number is fitted using a Voigt function (solid line), from which the amplitude of the Gaussian noise component is extracted.

ration. To initialize the atomic states with only the left sites occupied, we remove atoms from the right sites using a short-time resonant light pulse that only affects the $|F = 2, m_F = -2\rangle$ states.

We precisely control and stabilize the superlattice phase to ensure accurate observation of the tunneling effect, especially for bonded atoms. Normally, the lattice depths are set to relatively large values, with $V_{s,l} \sim \hbar \times 50$ kHz, while the energy difference Δ between the left and right sites should be maintained below the tunneling strength J_n , i.e., $\sim \hbar \times 50$ Hz. This phase stability is crucial for observing tunneling effects of atomic clusters with higher mass. To minimize phase fluctuations, we stabilize the optical lattice by integrating a significant portion of the retro-reflected optical path within the vacuum chamber, reducing environmental impacts from temperature and humidity variations.

To calibrate the phase stability of the optical lattice, we use single-atom tunneling to measure energy biases between double wells and extract phase fluctuations. Atoms are initialized to occupy the left site, with superlattice parameters set to $V_l = 8.87(4)E_r$ and $V_s = 27.33(5)E_r$, corresponding to a barrier height of $V_0/k_B = 4.32(1)$ μ K and a tunneling strength of $J_0/h = 10.0(2)$ Hz. After letting the system evolve for 25 ms, equivalent to half a tunneling period, we detect the atoms on the right site. The resulting spectroscopic measurements, shown in Fig.S3, exhibit broadening due to phase fluctuations.

The spectroscopy can be well fitted by a Voigt profile, a convolution of a Cauchy-Lorentz distribution and a Gaussian distribution. The full width at half maximum (FWHM) of the Lorentzian component is $40(1)$ Hz, determined by the Rabi bandwidth of the tunneling process.

From this, the Gaussian component, arising from fluctuations in the energy bias, is inferred to have an FWHM of $23(1)$ Hz. The corresponding relative fluctuation of the energy bias Δ/V_0 is $2.5(1) \times 10^{-4}$, sufficient for tunneling observations in large-mass clusters.

Our *in situ* imaging of the 2D atomic cloud provides insights into the spatial distribution of the superlattice potential. To characterize the spatial variations, we employ an entangled state and perform a Ramsey sequence to quantify energy offsets. Atoms are initialized in the superposition state $(|1, 0\rangle + i|0, 1\rangle)/\sqrt{2}$ and held for varying durations under lattice depths of $V_s = 30.90(5)E_r$, $V_l = 8.87(4)E_r$, and $V_y = 38.8(3)E_r$. A second Ramsey pulse is then applied, allowing the atoms to tunnel for another quarter period. The number of atoms that tunnel to the right lattice sites is measured, yielding N_R .

This Ramsey method enables high-resolution energy detection. As illustrated in Fig. S4, spatial variations in the energy shift Δ manifest as striped patterns. In certain double-well units, the phase of the superposition state oscillates over time, indicating an energy imbalance between the two wells. This imbalance, Δ , exhibits a spatial distribution $\Delta(x, y)$ across the lattice. By analyzing the standard deviation of atomic density, we estimate a pattern decay lifetime of $22(2)$ ms, partially attributed to decoherence. The spatial variation in $\Delta(x, y)$ is around $\hbar \times 45(5)$ Hz, corresponding to a relative variation of $3.0(3) \times 10^{-4}$ compared to the lattice depth of approximately $\hbar \times 150$ kHz along the x - or y -directions.

Since our measurements are averaged over multiple double-well units, spatial inhomogeneity in the potential limits coherence. Variations within double wells lead to enhanced apparent decay effects when averaging over larger regions, primarily due to the trapping potential

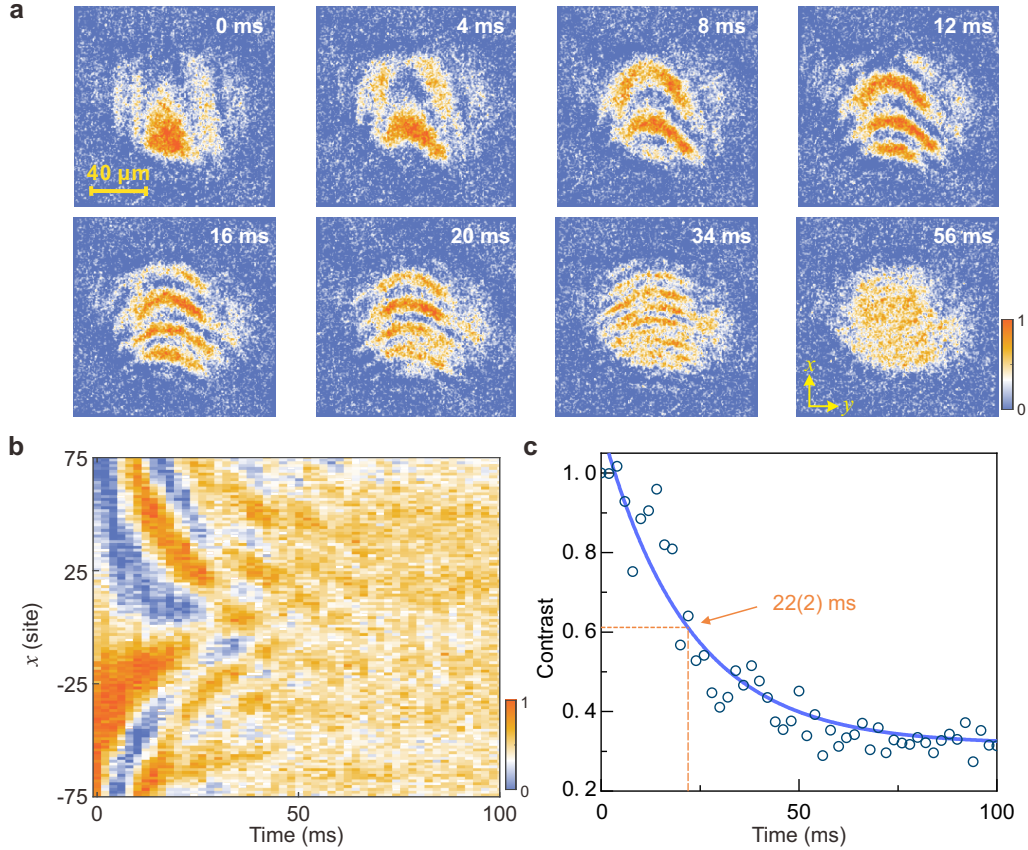


FIG. S4: Probing the spatial distribution of $\Delta(x, y)$. We generate single-atom entangled states in double-well units, specifically $(|1, 0\rangle + i|0, 1\rangle)/\sqrt{2}$, and hold them in deep optical lattices for time t_R . In each double-well, the energy bias $\Delta(x, y)$ induces a phase shift to the state, evolving the state to $[|1, 0\rangle + \exp(i[\Delta(x, y)t_R/\hbar + \pi/2])|0, 1\rangle]/\sqrt{2}$. A second $\pi/2$ pulse via tunneling completes the Ramsey sequence for phase measurement. (a) Spatially resolved Ramsey measurements. The distribution of Δ in the x - y plane is shown at different times, revealing spatial energy shifts that reflect potential inhomogeneity. Averaging over a certain region leads to effective dephasing of the entangled state. (b) Time-resolved measurements of the distribution of Δ . The spatial signal in (a) is averaged over 21 sites along the y -direction, revealing inhomogeneity along the x -axis. The contrast of the pattern decays over time. (c) Decay of contrast and the lifetime of the pattern. To evaluate the contrast of the pattern, we calculate the standard deviation of the measurements from the pattern and plot the contrast as a function of time, revealing a $1/e$ lifetime of 22(2) ms.

envelope and local disorder. This explains the reduced coherence time observed when averaging over the entire atomic cloud, as discussed in Ref. [5]. To mitigate spatial inhomogeneity, we employ the 1064 nm pancake lattice to compensate this effect. Meanwhile, we leverage the spatial resolution of *in situ* imaging to analyze regions with uniform experimental parameters. This Ramsey method serves as a precise tool for mapping system homogeneity, making our optical lattice platform well-suited for exploring many-body physics.

To further understand decoherence mechanisms in the tunneling process, we extract decay times from tunneling dynamics in the central region of the cloud. Here, an increase in atom number n in the tunneling dynamics leads to a reduction in coherence time, as shown in Fig.2e. The coherence time as a function of atom number is plotted in Fig.S5. For an NOON state, which can

be viewed as a maximally entangled Greenberger-Horne-Zeilinger (GHZ) state, $(|n, 0\rangle + i|0, n\rangle)/\sqrt{2}$, any single-particle decoherence leads to the collapse of the entire state. The energy offset Δ affects the n -th order tunneling process by a factor of n , making large clusters more sensitive to energy imbalances. Fig. S5 shows that the coherence time of tunneling dynamics scales approximately as $1/n$, suggesting that decoherence primarily originates from single-particle effects. The coherence time of the tunneling dynamics is nearly twice that of the entangled state, as the atoms remain in the entangled state for only half of the tunneling cycle. For even higher-mass clusters, correlated noise may introduce additional decoherence to this maximally entangled state.

Compared to other high-order processes in spin-exchange [22] or ring-exchange experiments [42], the relatively long coherence times observed in prior work can

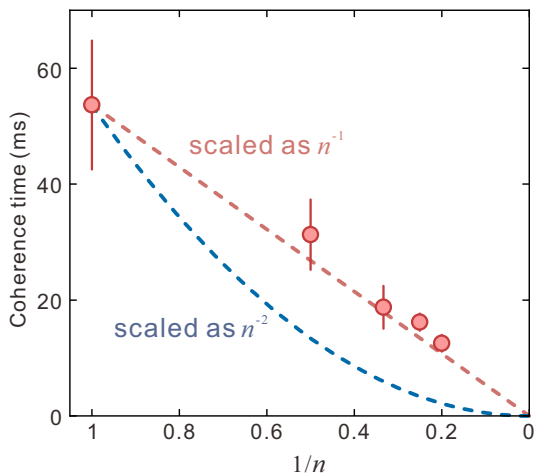


FIG. S5: Coherence of the quantum tunneling dynamics. The coherence time of atomic clusters is extracted from the tunneling oscillations shown in Fig. 2e and plotted as a function of $1/n$. The maximally entangled NOON state is prepared at the quarter period of these oscillations. The dashed lines serve as guides to the eye, with the red line indicating a decay proportional to $1/n$ and the blue curve corresponding to a decay proportional to $1/n^2$. Our experimental data closely follows the $1/n$ decay trend.

partly be attributed to the absence of atomic center-of-mass motion. In spin-entangled states, atomic masses remain balanced across lattice wells. In contrast, our entangled state is spatially distributed with a separation of approximately 320 nm. Detecting the state $(|n, 0\rangle + i|0, n\rangle)/\sqrt{2}$ results in spatially separated outcomes $|n, 0\rangle$ or $|0, n\rangle$, with their centers separated by 320 nm. This spatial distribution enhances the sensitivity of the state to spatial disturbances and energy inhomogeneities. While maintaining coherence in such states presents technical challenges, it also offers significant advantages for precisely measuring spatial energy differences.

THEORETICAL SIMULATIONS

The seminal work of Ref. [2] established that the transmission probability of particles through a barrier decreases exponentially with mass, following the relation of $\exp(-\gamma\sqrt{m})$. In our optical lattice system, the tunneling strength for single atoms or tightly bound molecules can be calculated using band theory. In the tight-binding regime, the tunneling strength J_0 , equivalent to a quarter of the ground-band bandwidth, is given by,

$$J_0 \simeq \frac{4}{\sqrt{\pi}} E_r \left(\frac{V_0}{E_r} \right)^{3/4} \exp \left[-2 \left(\frac{V_0}{E_r} \right)^{1/2} \right]. \quad (\text{S1})$$

This leads to the same exponential dependence of the tunneling strength on both the particle mass and the

barrier height,

$$J_0 \propto (m)^{-1/4} \exp[-\gamma\sqrt{m}], \quad \gamma = \frac{2\sqrt{2V_0}\lambda_s}{h}. \quad (\text{S2})$$

This exponential decay of tunneling strength, even in ultracold atomic systems, presents significant challenges for observing quantum tunneling of objects with large masses. Prior to this work, this behavior was generally considered an intrinsic and invariable property.

We propose that when atoms form weakly bonded clusters, the tunneling strength transitions from an exponentially suppressed regime to near-unity scaling. This transition can be understood using high-order perturbation theory. In the regime where the tunneling strength J_0 is much smaller than the on-site interaction U ($J_0 \ll U$), the effective Hamiltonian for the clusters can be derived. Taking a five-atom cluster as an example, the tunneling strength is determined by the matrix element,

$$\langle 0, 5 | \hat{H}_c | 5, 0 \rangle = \frac{\prod_{i=0}^4 \langle 4-i, i+1 | \hat{H}_0 | 5-i, i \rangle}{\prod_{i=1}^4 (E_{|5,0\rangle} - E_{|5-i,i\rangle})}. \quad (\text{S3})$$

As shown in Fig.2b, four intermediate virtual states couple the initial state $|5, 0\rangle$ to the final state $|0, 5\rangle$. The prefactor α_n decreases with increasing cluster size due to the growing differential on-site energy, where the minimum energy gap for an n -atom Mott insulator is $(n-1)U$. Meanwhile, bosonic enhancement amplifies the coupling strength. For the five-atom cluster, these competing effects yield a coefficient of $5/24$. Table I summarizes the coefficients for different cluster sizes, expressed as J_0^n/U^{n-1} . This perturbative process provides an additional pathway for tunneling dynamics.

n	1	2	3	4	5
coefficient	1	2	3/2	2/3	5/24

TABLE I: Tunneling coefficient of n -atom clusters

In the strongly bonded regime, where J_0 is many orders of magnitude smaller than U , the coupling strength J_0^n/U^{n-1} becomes negligible, and tunneling primarily arises from the collective motion of the bonded massive cluster.

For weakly bonded clusters, we depart from the perturbative regime, particularly when $J_0/U \sim 1$. In this case, tunneling dynamics can be computed using exact diagonalization of the Bose-Hubbard Hamiltonian. Taking the five-atom cluster as an example, the Hamiltonian matrix is given by,

$$\hat{H}_0 = \begin{pmatrix} 10U & -\sqrt{5}J_0 & 0 & 0 & 0 & 0 \\ -\sqrt{5}J_0 & 6U & -2\sqrt{2}J_0 & 0 & 0 & 0 \\ 0 & -2\sqrt{2}J_0 & 4U & -3J_0 & 0 & 0 \\ 0 & 0 & -3J_0 & 4U & -2\sqrt{2}J_0 & 0 \\ 0 & 0 & 0 & -2\sqrt{2}J_0 & 6U & -\sqrt{5}J_0 \\ 0 & 0 & 0 & 0 & -\sqrt{5}J_0 & 10U \end{pmatrix} \quad (\text{S4})$$

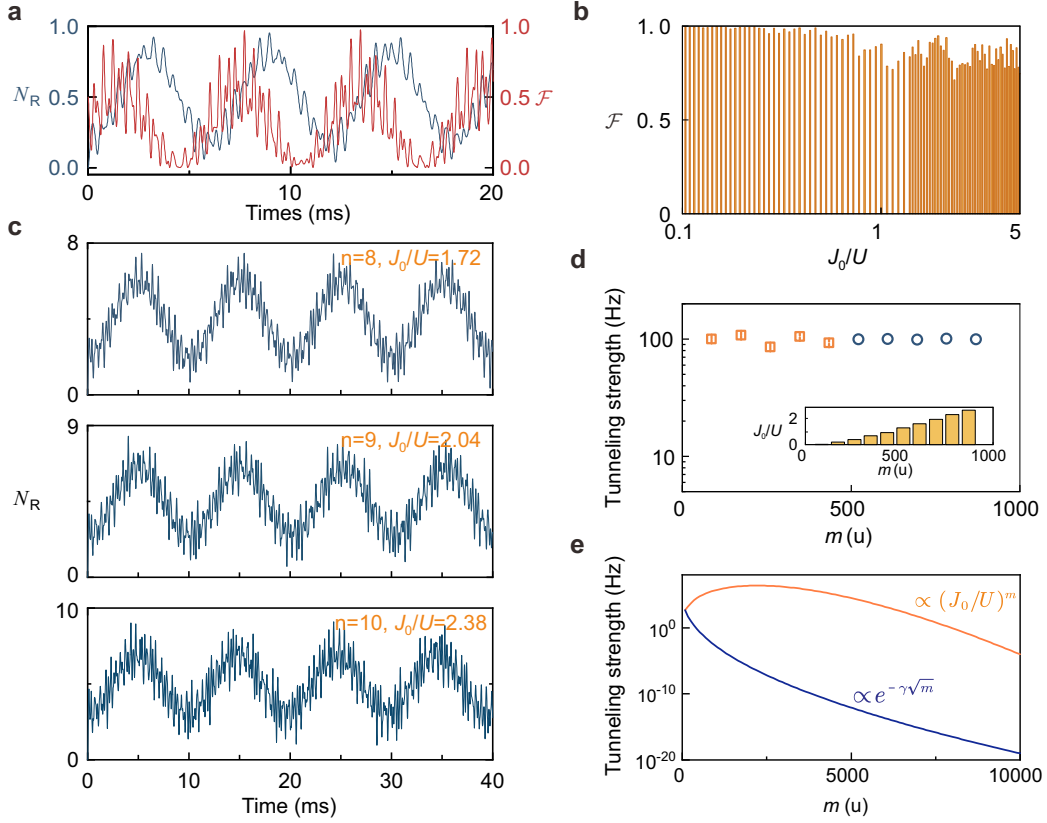


FIG. S6: Theoretical simulations. (a) Tunneling dynamics of $n = 5$ bonded cluster. We simulate the tunneling dynamics of a $n = 5$ bonded cluster with a coupling ratio $J_0/U = 0.94$. The atom number on the right site is plotted as the blue curve, while the red curve shows the fidelity for preparing the entangled state $(|5, 0\rangle + i|0, 5\rangle)/\sqrt{2}$. (b) Fidelity for NOON state at various coupling strengths. As the coupling strength J_0/U increases, the system moves away from the perturbation regime. Despite this, the fidelity for realizing the NOON state remains considerably high even at $J_0/U = 5$. (c) Tunneling dynamics for larger clusters ($n = 8, 9, 10$). For these clusters, we optimize the J_0/U parameters to achieve tunneling oscillations with appropriate frequency for experimental measurement. (d) Tunneling strength for atomic clusters with up to 10 atoms. The ratio J_0/U is tuned to appropriate values as shown in the inset. The tunneling strength is plotted, with orange squares denoting experimental measurements and blue circles representing theoretical calculations. (e) Tunneling dynamics for even larger clusters. Using high-order perturbation theory, we calculate the tunneling strength based on Hamiltonian 2 by taking account of $J_n = \alpha_n J_0^n / U^{n-1}$ and the boson enhancement. Assuming the cluster mass can be increased up to $m = 10^4$ u, the tunneling strength can be smoothly adjusted by setting J_0 to approximately match the energy gap of the Mott insulating state, following the relation $J_0 = (n - 1)^{3/4} U$ for $n \geq 2$.

We numerically evolve the system under the Hamiltonian $|\psi(t)\rangle = \exp(-i\hat{H}_0 t/\hbar)|\psi(0)\rangle$ in the Fock-state basis. For multi-atom tunneling, density-induced tunneling effects further enhance the tunneling strength as the atom number increases.

Given the presence of decoherence, we describe the system using the density matrix ρ , and quantify the fidelity of the NOON state as $\mathcal{F} = \langle \psi_{\text{NOON}} | \rho_{\text{exp}} | \psi_{\text{NOON}} \rangle$, where for a five-atom cluster $|\psi_{\text{NOON}}\rangle = (|5, 0\rangle + i|0, 5\rangle)/\sqrt{2}$. In the absence of decoherence, Figure S6a presents the fidelity of the five-atom NOON state, while Fig. S6b shows the optimal fidelity across different J_0/U ratios. Notably, a fidelity of 90.3% is achievable even at $J_0/U = 3$. We incorporate decoherence effects by introducing a decay rate on the off-diagonal elements of the density matrix.

Our experimental results show excellent agreement with theoretical predictions. In Fig.2e, high-frequency oscillations from lower-order processes appear in the data. Imperfections in the Mott insulator state lead to additional occupations in some double wells. These effects can be accounted for by integrating the contribution of each double well, weighted by the fraction of imperfect components. Slight deviations in the coefficients, as shown in Table I and Fig.3a, arise when the parameters extend beyond the perturbative regime, leading to small shifts in the energy gap between eigenstates as J_0/U approaches 1. Additionally, coherence times inferred from damped sinusoidal fits are incorporated into the theoretical analysis in Fig.2e.

To explore tunneling dynamics in larger clusters, we extend our simulations to higher masses (e.g., $n =$

8, 9, 10). Assuming an on-site interaction of $U/h = 800$ Hz, we adjust the tunneling strength J_0 to optimize the tunneling strength. As shown in Fig. S6c, the dominant oscillations correspond to the tunneling of bonded clusters. Despite the presence of higher-frequency oscillations arising from lower-order processes, the collective tunneling of the entire cluster remains within the experimentally accessible regime. NOON states maintain high fidelity around the quarter-period evolution, confirming the feasibility of scaling to 10 atoms with a total mass of 870 u. In principle, as J_0 approaches the minimum energy gap $(n-1)U$ of an n -atom Mott insulator, the tunneling strength of bonded clusters should continue to increase. As depicted in Fig. S6e, this scaling suggests that total masses up to 10^4 u can be reached by tuning J_0 to $(n-1)^{3/4}U$ for $n \geq 2$. As is well known, much larger clusters may introduce additional constraints: the on-site interaction can exceed the barrier height, invalidating the two-body interaction approximation, increasing loss rates, and shortening coherence time. However, our current focus is to identify a regime where tunneling of larger-mass clusters remains observable.

ENTANGLEMENT OF POSITION STATES AND QUANTUM ENHANCED MEASUREMENTS

Precision measurements can reach their ultimate limit through quantum entangled states, such as the NOON state, which exploits quantum superpositions of N indistinguishable particles. This enables measurements to approach the Heisenberg limit, achieving precision $\Delta\theta = 1/N$ that surpasses the standard quantum limit of $\Delta\theta = 1/\sqrt{N}$. NOON states have been successfully realized experimentally in photon [28, 29, 43, 44] and phonon [45] systems. However, prior to this work, the creation of massive NOON states involving more than two atoms has yet to be achieved. Unlike photons, massive particles are more susceptible to a wider range of interactions, making the generation of NOON states considerably more challenging, particularly those with spatial separation. However, this sensitivity also enables significant enhancements in measurement precision, with potential applications in gravity sensing [27] and fundamental tests of quantum mechanics [39].

We generate the entangled state through quantum tunneling, with the fidelity inferred from its oscillation amplitude. The atomic clusters are initially prepared on the left sites and allowed to tunnel for a quarter period. During tunneling, the atoms bond into clusters and tunnel as a single entity, avoiding distinct population of intermediate virtual states. Even in the $J_0/U \sim 1$ regime, high-fidelity NOON states with large n can be achieved by optimizing the tunneling time. For example, a 1.23 ms tunneling time results in a 90.6% fidelity for the $(|5, 0\rangle + i|0, 5\rangle)/\sqrt{2}$ state (see Fig.S6a).

In the experiment, population leakage to unwanted states and decoherence effects reduce the fidelity of the entangled state $(|5, 0\rangle + i|0, 5\rangle)/\sqrt{2}$. Taking into account the imperfections of the Mott insulator and the fluctuations of the experimental parameters, the fidelity of the entangled state predicted by theoretical simulations aligns with the Ramsey measurement, producing a limited oscillation amplitude of 0.52(3), as shown in Fig. 4b.

To characterize the quantum entangled state for quantum metrology, we utilize Fisher information to assess its precision (Fig. 4). Fisher information is generally expressed as [27],

$$F(\theta) = \sum_{\mu} \frac{1}{P(\mu|\theta)} \left(\frac{\partial P(\mu|\theta)}{\partial \theta} \right)^2, \quad (\text{S5})$$

where μ denotes the eigenvalue of an observable and $P(\mu|\theta)$ represents the associated probability. In our system, the parity of the atoms serves as the observable, which means right site has the parity +1, and the left site has parity -1. For a pure NOON state, $|\psi_{\text{NOON}}\rangle = [|n, 0\rangle + e^{i(n\theta+\pi/2)} |0, n\rangle] / \sqrt{2}$, the probability after applying the second Ramsey $\pi/2$ pulse is,

$$P(\mu = \pm 1|\theta) = \frac{1 \pm \cos n\theta}{2}. \quad (\text{S6})$$

The Fisher information for this pure NOON state is $F(\theta) = n^2$, which is n times the standard quantum limit. In this context, the quantum Cramér-Rao bound [26, 27] gives the maximum phase sensitivity as, $\Delta\theta = 1/\sqrt{F(\theta)} = 1/n$. In practice, experimental noise and decoherence reduce the Fisher information, which is related to the visibility of the parity oscillation. In our Ramsey measurements, the parity oscillation amplitude is,

$$P(\mu = \pm 1|\theta) = \frac{1 \pm A \cos n\theta}{2}, \quad (\text{S7})$$

where $0 \leq A \leq 1$ is the visibility. The Fisher information is then given by,

$$F(\theta) = \frac{A^2 n^2 \sin^2 n\theta}{1 - A^2 \cos^2 n\theta}. \quad (\text{S8})$$

The Fisher information reaches its maximum value $F = A^2 n^2$ when $\sin n\theta = \pm 1$.

We demonstrate quantum precision measurements beating the standard quantum limit using Fisher information. A spatially distributed staggered potential is introduced via a spin-dependent optical superlattice, inducing an energy bias of $\Delta/h = 1.49(2)$ kHz between the left and right sites. The entangled states evolve in this staggered potentials, accumulating a phase $n\theta$. The phase is then projected onto the atom number imbalance between the two sites through a second Ramsey $\pi/2$ -pulse.

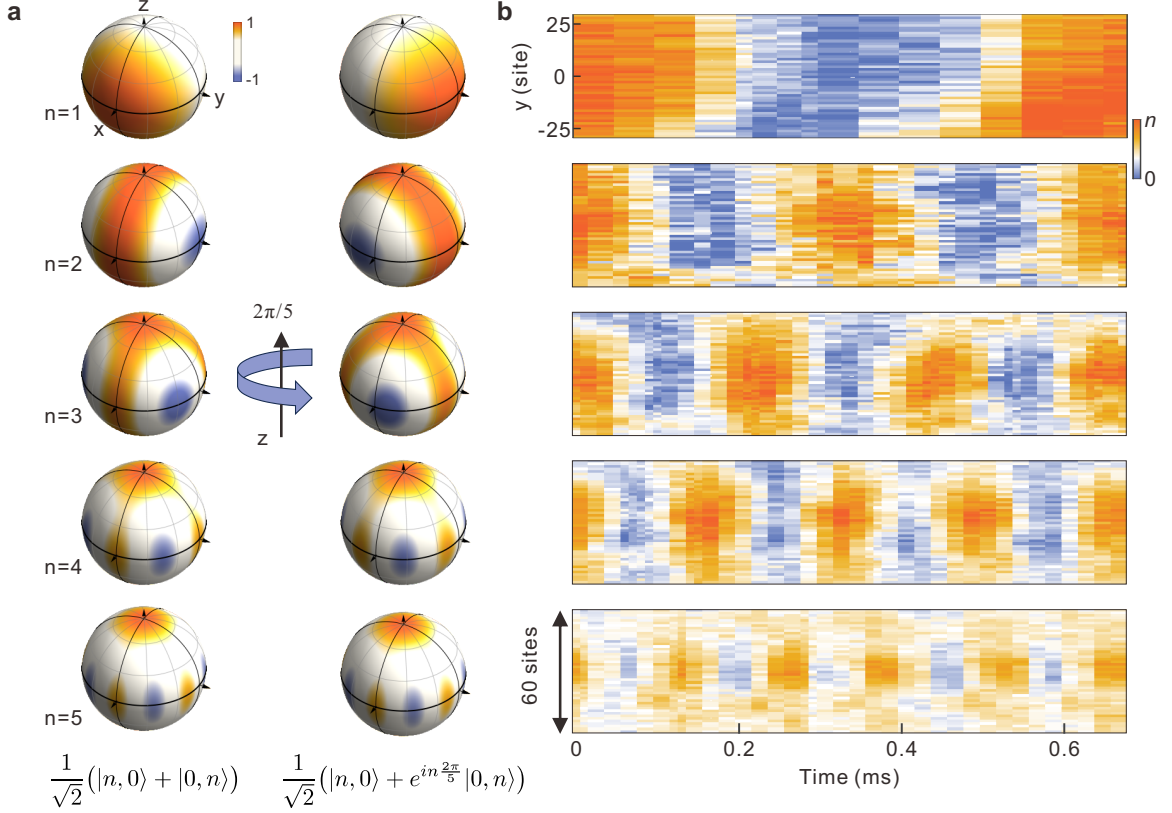


FIG. S7: Spatial distribution of Ramsey interferometry. (a) The normalized Wigner distribution on the Bloch sphere illustrates the NOON state for various values of n . The distribution demonstrates that rotating the state by $2\pi/n$ around the z -axis restores the initial n -atom NOON state. The left panel shows the initial NOON states, while the right panel displays their distributions after a $2\pi/5$ rotation. (b) Ramsey interferometry reveals phase information, which can be inferred from the atomic population. The spatial pattern and oscillations are clearly visible in the measurements, which is shown with atomic density in right sites. This method enables the detection of micrometer-scale spatial energy shifts.

From the measurements in Fig. 4, we extract the oscillation amplitude of the parity (imbalance) A and derive the Fisher information $F = A^2 n^2$. The standard quantum limit corresponds to measurements with n copies of the superposition state $(|1, 0\rangle + i|0, 1\rangle)/\sqrt{2}$. Using single entangled states, the Fisher information values achieved are 2.5(1), 5.6(2), 7.6(3), and 6.2(7) for clusters with $n = 2, 3, 4$, and 5, respectively. The derived phase sensitivities $\Delta\theta$ are, respectively, 0.64(2), 0.42(1), 0.36(1), and 0.40(2). For the four-body NOON state, this results in a 1.4(1) dB enhancement in phase sensitivity beyond the standard quantum limit, confirming the improved precision achievable in quantum metrology.

Even when assessing the standard quantum limit, the superposition state itself is a quantum resource. For detecting energy shifts within a given double-well region, a single-atom superposition state should define the standard quantum limit, rather than n independent copies of such states. With sufficient atoms in the cold ensemble, the main challenge is their distribution into the required double-well regions, as increasing independent

copies without spatial constraints does not improve precision. Thus, Fisher information exceeding 1 confirms an advantage over classical methods (see Fig. 4c). In this sense, our experiment achieves a larger enhancement in measuring this specific energy shift, achieving 8.8(2) dB in Fisher information. Moreover, this demonstrates that our cold-atom-based approach enables a scalable method for quantum sensing of spatially distributed fields.

Finally, we observe spatially distributed oscillation patterns in quantum precision measurements (Fig. S7). The central region shows the expected frequency scaling linearly with n , while phase shifts occur at the periphery, due to preparation inhomogeneities and spatial variations in the energy field. The oscillation frequency can be determined with high accuracy, making the NOON state suitable for measuring various interactions and energy shifts. To further enhance precision, optical tweezers could be employed to separate the atomic cluster into larger distance, thereby improving sensitivity to fields such as gravity.